

Landslide Inventory Mapping Based on Independent Component Analysis and UNet3+: A Case of Jiuzhaigou, China

Xuerong Chen^{1b}, Student Member, IEEE, Chaoying Zhao^{1b}, Senior Member, IEEE,
Zhong Lu^{1b}, Senior Member, IEEE, and Jiangbo Xi^{1b}, Member, IEEE

Abstract—Landslide inventory mapping (LIM) is an important prerequisite for disaster emergency rescue and landslide sensitivity analysis. It has been proven that convolutional neural networks have better performance for LIM than traditional machine learning methods such as support vector machines, and random forests. However, the accuracy of existing methods based only on optical images is low due to the complex landslide background. Moreover, the multiscale features of landslides are not considered in convolutional neural network methods. Therefore, this study proposes multifeatured independent component analysis UNet3+ for landslide inventory mapping based on optical images, which combines co-feature, independent component analysis (ICA), and UNet3+. First, normalized difference vegetation index (NDVI) and gray level co-occurrence matrix (GLCM) are extracted from remote sensing images acquired pre- and postearthquake event and then processed by change vector analysis. Then, ICA is implemented for NDVI, GLCM, and three elevation factors. Finally, the three principal components and the postevent images are fed into UNet3+ to generate LIM by multiscale features and deep supervision. Finally, we validate the proposed method by using the coseismic landslide of Jiuzhaigou earthquake as an experiment. The results show that the performance of recall, F1-score and mIoU are 0.13, 0.22, and 0.11 higher than those of the postevent-only images, respectively, indicating that the proposed method can effectively solve the problems of landslide identification in terms of multiscale features and complex background.

Index Terms—Deep learning, independent component analysis, landslide inventory mapping, remote sensing, UNet3+.

I. INTRODUCTION

EARTHQUAKES, typhoons, and heavy rainfall events usually cause numerous geological hazards, such as landslides and debris flows [1], [2], [3]. Landslides are one of

Manuscript received 7 May 2023; revised 17 July 2023; accepted 9 October 2023. Date of publication 5 December 2023; date of current version 3 January 2024. This work was supported in part by the National Key Research and Development Program of China under Grant 2022YFC3004302, in part by the National Natural Science Foundation of China under Grant 41929001, and in part by Chang’an University High Performance Computing Platform. (Corresponding author: Chaoying Zhao.)

Xuerong Chen, Chaoying Zhao, and Jiangbo Xi are with the School of Geological Engineering and Geomatics, Chang’an University, Xi’an 710054, China (e-mail: xuerongchen@chd.edu.cn; cyzhao@chd.edu.cn; xijiangbo@chd.edu.cn).

Zhong Lu is with the Roy M. Huffington Department of Earth Sciences, Southern Methodist University, Dallas, TX 75275 USA (e-mail: zhonglu@mail.smu.edu).

Digital Object Identifier 10.1109/JSTARS.2023.3339295

these catastrophic chain hazards, often causing road blockages, lake damming, infrastructure damage, and serious casualties. Landslides are occurring with increasing frequency as extreme weather events increase around the world [4], [5], [6]. Comprehensive and reliable landslide inventory mapping (LIM) triggered by these extreme events are a prerequisite for emergency rescue and disaster mitigation [7].

Big remote sensing data including optical satellite images [8], airborne light detection and ranging (LiDAR) [9], and synthetic aperture radar (SAR) images [10] makes LIM more applicable and reliable than ever before [11]. Landslides triggered by events are highly destructive to the surface coverage, especially in vegetated areas [12]. We can identify landslide scars from remote sensing images by morphology and texture rather than field investigations, which is much effective, especially for large-scale landslide investigations [7].

On the other hand, deep learning methods, such as convolutional neural networks (CNNs) have been verified to be more applicable and effective in LIM compared to traditional pixel-based methods [13], [14], [15], and the object-oriented approaches [16], [17], [18], [19]. And the visual interpretation of remote sensing images of the landslide as the most accurate method turns into the essential reference label in deep learning LIM [20], [21].

Deep learning architectures based on CNNs have changed the means to extracting information from images. In recent years, this method has also been used for LIM. Ghorbanzadeh et al. [22] first compared the application of different machine learning methods such as support vector machines, and random forests (RF), and CNN in landslide detection and proved that CNN was superior to traditional machine learning methods. Because of the lack of landslide samples, Meena et al. [23] proposed to use of K-fold cross-validation to improve the sample utilization rate and improve the accuracy of landslide inventory mapping. Ji et al. [24] established an open database in Bijie, China. After validation, the CNN model based on the digital elevation model (DEM) attention mechanism has the best accuracy. Yi and Zhang [25] designed a data augmentation strategy of automatic generation of training samples to alleviate the problem of insufficient training samples. And a cascading end-to-end deep learning network LandsNet was constructed to learn various characteristics of landslides.

Shi et al. [26] used change detection and CNN to catalog landslides and further extracted landslide elements. Deep learning is just at the beginning stage to be used for landslide inventory mapping.

Currently, more semantic segmentation algorithms are used to map landslide inventory. Qi et al [27] and Liu et al [28] used ResU-Net and modified U-Net for landslide extraction, respectively. Zhang et al. [8] used the deep learning module in ENVI software for landslide cataloging and discussed the accuracy of different parameters. However, the information provided by optical images is limited, and features related to landslides can improve the accuracy of landslide mapping. Nava et al. [29] modified an Attention U-Net and used it to evaluate two and three Sentinel-1 satellite images to map landslides even under thick cloud coverage conditions.

In addition, researchers have explored the potential of normalized difference vegetation index (NDVI), DEM and other factors combined with CNN in various landslide detection tasks [30], [31]. Gao et al. [32] used fully convolutional densenet (FC-DenseNet) for LIM and explored the importance of different features for LIM. By enhancing the samples with background, Soares et al. [33] used RapidEye satellite images, NDVI and DEM to create the dataset. They found that the NDVI layer was beneficial to the balance of the model, and the morphological post-processing operation improved effectively the segmentation accuracy. Yang et al. [34] proposed a model to reduce the false extraction of background objects. Considering the complex background and the diversity of remote sensing images, Chen et al. [35] recently proposed squeeze-and-excitation network for feature fusion to improve the shortcomings of traditional UNet. They achieved good results using Sentinel-2 images for landslide extraction. The environment of a disaster area plays a leading role in the landslide formation process, so environment induced attributes including DEM, slope, and distance to the river are used as supplements to provide additional information for landslide extraction model and further improve the accuracy of landslide extraction. Combining the topographic factor and spectral information to train the data set helps to compare the landslide with other similar features, as demonstrated by Ghorbanzadeh et al [36]. Wang et al. [37] proved that principal component analysis multifeature and ensemble strategy can improve the accuracy of coseismic landslide extraction. The previous studies showed that the multi-feature could assist CNN to better perform in the landslide inventory mapping.

The optimization of network structure and training data can improve the extraction accuracy of landslide to a certain extent. The inclusion of assisted information can also bring noise, so it is critical to suppress the nonrelated information and increase the landslides related information. In other words, it is worth exploring to enhance the heterogeneity between classes while improving intra-class homogeneity. Simultaneously, it is difficult to achieve accurate landslide mapping on a large area only relying on shallow or deep features. In this study, the multifeatured independent component analysis and UNet3+ (MICUNet3+) method is proposed for landslide inventory mapping, where UNet3+ was used to perform LIM through

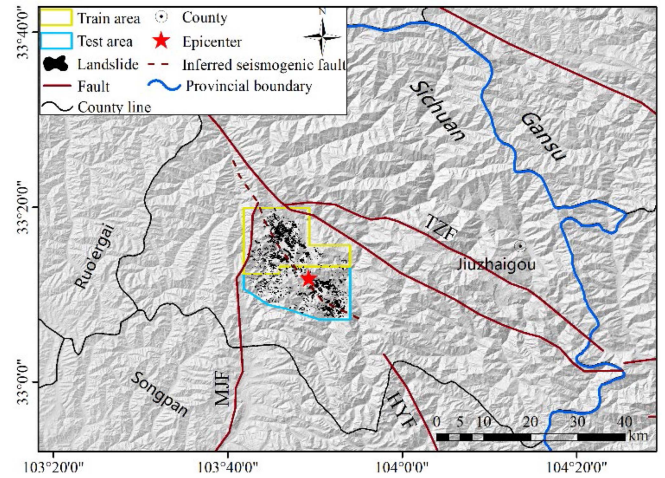


Fig. 1. Background of the study area. Yellow represents landslides. The yellow and blue polygons represent the training and testing areas in this study. The red dashed line represents the inferred seismogenic fault. The solid red lines represent active faults. TZF, MJF, and HYF represent the Tazang fault, Minjiang fault, and Huya fault, respectively.

independent component analysis (ICA) combined with optical image derived features, topography, and other factors. The main contributions of the proposed MICUNet3+ are as follows.

- 1) A total of 13 cofactors, which are topographic features (elevation, slope, and gradient), NDVI, and nine gray level co-occurrence matrix (GLCM) features derived from the optical images, were used to assist UNet3+ in LIM. It reduces the influence of complex backgrounds of optical images.
- 2) ICA was used to analyze 13 cofactors, which can improve the intraclass homogeneity and enhance the interclass heterogeneity, to reduce the impact of noise caused by multifeatures.
- 3) A deep supervised UNet3+ with multiscale feature skip connections was used to adjust to the multiscale characteristics of landslides. Meanwhile, the deep supervision processing also helps to reduce the impact of a complicated background.

The objective of this study is to perform rapid and accurate postevent LIM using optical image. Derived from optical images and topographic features were used to assist postevent image to improve the accuracy of LIM. To suppress the adverse effect of noise on the feature factors, ICA was used to enhance the discrimination between landslides and nonlandslides. UNet3+ was used to consider the characteristics of multiscale landslides and complex backgrounds. For validation, landslides identification after the 2017 Jiuzhaigou earthquake in China was tested with MICUNet3+ and satellite images. In this study, the effectiveness of the proposed method was verified by comparing it with different feature processing methods.

II. STUDY AREA

The study area is located in Jiuzhaigou County, Sichuan Province, China (see Fig. 1). The elevation is less than 2000 m a.s.l. in the north and more than 4800 m a.s.l. in the south,

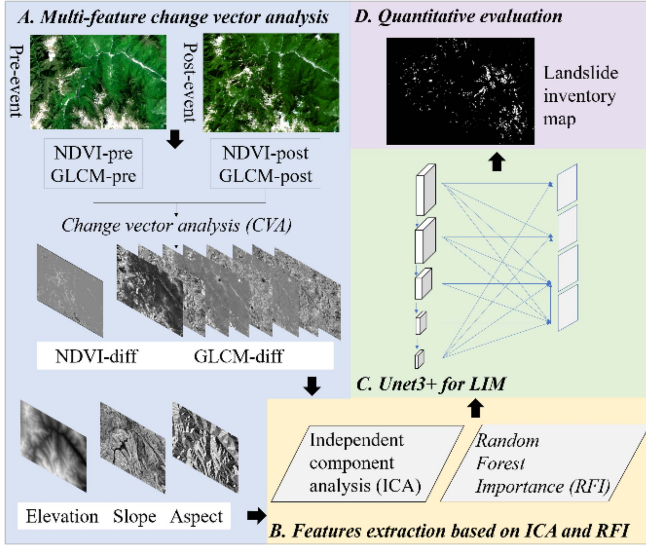


Fig. 2. Flow chart of MICUNet3+ used in this study.

including high alpine and valleys. Numerous faults, such as the NS-trending reverse thrusting Minjiang fault (MJF), the NWW-directed strike-slip Tazang fault (TZF), and some secondary faults are developed in this region. Rainfall in Jiuzhaigou is less than 600 mm annually low but concentrated, and July to August are typical rainy seasons.

On August 8, 2017, an $MW6.5$ ($Ms7.0$) earthquake occurred in Jiuzhaigou County with a focal depth of 20 km. The epicenter was centered near the MJF fault, TZF fault, and Huya fault (HYF) (see Fig. 1), according to the China Earthquake Administration. The inferred seismogenic fault is NW trending, based on a field investigation of surface deformation by Li et al. [38]. Xu et al. [2] identified coseismic landslides (see black polygons in Fig. 1) by visual interpretation based on GeoEye-1 satellite images, of which the maximum area was 236338.3 m², the minimum area was 7.8 m², and the average area was 1993.4 m². This study refers to the research results of Xu et al. [2], and the landslide interpretation is accurate, which ensures the reliability of the results of this study.

The training area is divided into the train set and validation set to feed into the UNet3+ network, where we crop through a sliding window and randomly assign it as the train set and validation set with a ratio of 8:2. It is to enrich the background of the samples to train the model and to outperform the prediction in the test area.

III. METHODOLOGY

The flow of the MICUNet3+ method for LIM is shown in Fig. 2. First, NDVI and GLCM including Mean, Variance, Standard, Homogeneity, Contrast, Dissimilarity, Entropy, Angular Second Moment, and Correlation, were derived from pre- and postevent optical images. And change vector analysis of NDVI and GLCM pre- and postevent was performed to obtain the difference of NDVI (NDVI-diff) and the difference in GLCM (GLCM-diff). Then ICA and random forest importance (RFI)

TABLE I
OVERVIEW OF RAW DATA AND DERIVED FEATURES

Feature	Pre-event	Post-event
Images	Landsat-8	Sentinel-2
Collected date	2014/06/01	2017/09/07
Resolution	15 m	10 m
Spectral	Blue(B2), Green(B3), Red (B4), NIR(B5)	Blue(B2), Green(B3), Red(B4), NIR(B8)
NDVI	(NIR-Red)/(NIR+Red)	
Texture	GLCM (Mean, Variance, Standard, Homogeneity, Contrast, Dissimilarity, Entropy, Angular Second Moment, Correlation)	
DEM	SRTM (30 m)	
Terrain	Slope, Aspect	

were performed separately on 13 cofeatures, including topographic features (elevation, slope, and aspect), NDVI-diff, and nine GLCM-diff. The postevent images and labels were fed into the Unet3+ network separately along with the first three principal components of ICA and the three features selected by RFI, respectively. Finally, the trained model was used to generate the LIM of the test area.

A. Multifeature Change Vector Analysis

In this study, optical images and DEM are selected as raw data. Cloud-free images of Landsat-8 (pre-event) acquired on June 1, 2014 and Sentinel-2 (postevent) acquired on September 7, 2017 were collected with similar seasonal characteristics (see Fig. 3).

The red, green, blue, and near-infrared (NIR) bands of Landsat-8 and Sentinel-2 images are used to derive NDVI and texture features (see Table I). The training and the test areas are determined according to the range of the extreme earthquake area (see Fig. 3) generated by Xu et al. [2]. For the purpose of detecting changes and ensuring spatial consistency of the analysis, we unified Landsat-8, Sentinel-2, and DEM into the WGS 1984 coordinate system and sampled them uniformly at a resolution of 15 m.

GLCM provides the gray direction, interval, and amplitude of the change of image, rather than different texture properties. Therefore, we use statistical attributes to describe texture features quantitatively. Nine commonly used statistical attributes of texture features are adopted for results validation, including mean, variance, standard, homogeneity, contrast, dissimilarity, entropy, angular second moment, and correlation.

B. Features Extraction Based on ICA and RFI

ICA converts a set of mixed signals into independent components [39]. The components are orthogonal and independent

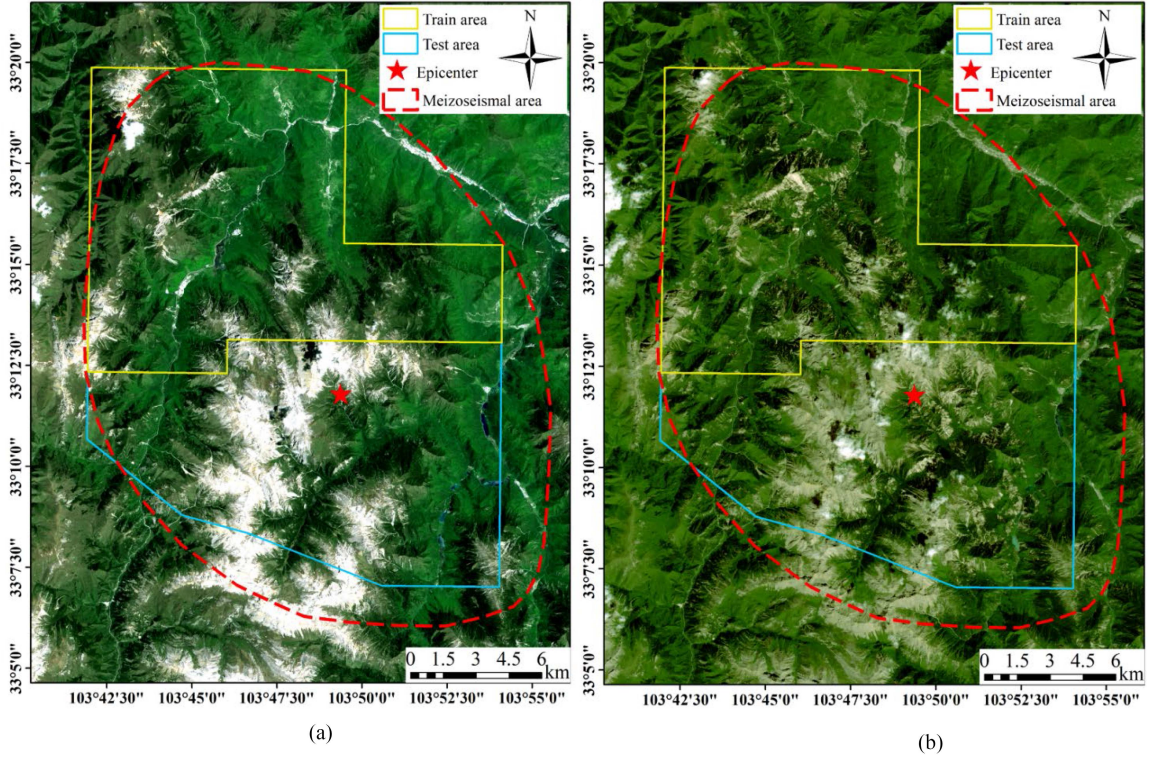


Fig. 3. Pre- and postevent remote sensing images over Jiuzhaigou earthquake. (a) Pre-event remote sensing image acquired on June 1, 2014. (b) Postevent remote sensing image acquired on September 7, 2017. The red dotted line indicates the extreme earthquake area.

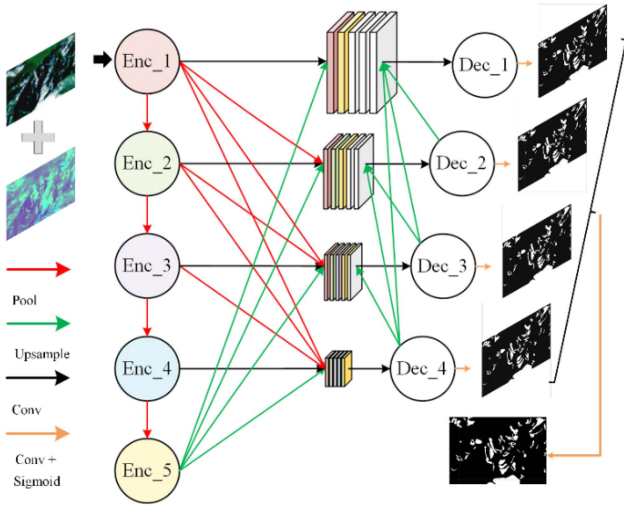


Fig. 4. Structure of UNet3+ for LIM, where Enc_1 to Enc_5 represent encoder, and Dec_1 to Dec_4 represent decoder.

of each other. The data are converted into independent parts (decorrelation) that can be used to detect and separate hidden noises, reduce dimensionality, and extract the main information in the image.

We represent the vector x as a linear combination of basis function A . As shown in (1), N represents the total number of image pixels, A_i is the column vector of the basis function matrix

A of i , and y_i is an element of the coefficient vector y

$$x = \sum_{i=0}^{N-1} A_i y_i. \quad (1)$$

The main purpose of ICA is to find a matrix of coefficients A , which makes the component coefficients y obtained after x transformation as independent as possible. The basic idea is to maximize the joint entropy of stochastic gradient ascent. The change of A during the iteration is as (2), where T denotes the transpose of the matrix

$$\Delta A = (I + (1 - 2/(1 + e^{-y})) y^T) A. \quad (2)$$

Before ICA training, x tends to its mean value and is multiplied by a white noise matrix. As shown in (3), where $A_0 = [(x - m_x)(x - m_x)^T]^{-1/2}$

$$x = A_0 (x - m_x). \quad (3)$$

Therefore, the whole transformation process can be considered as the product of the whitening matrix A_0 and the ICA training matrix, i.e., $W_I = W W_0$. Finally, the ICA matrix is orthogonalized to obtain

$$A = A_I (A_I^T A_I)^{-1/2}. \quad (4)$$

When the ICA transformation matrix is used as the basis for image projection, the basis function must be orthogonal. The rows of A are definitely orthogonal to each other. And the number of basis functions is the same as the number of elements in each basis function.

Random forest importance (RFI) is to calculate the influence of unselected data on the current decision tree in each decision tree of the random forest [40], namely out-of-pocket error (errOOB1). The errOOB2 is calculated for adding noise interference to out-of-bag (OOB) data. The larger the difference, the more important the feature is to the model [41].

OOB data refers to the data that is not selected in the training set. Each time about 1/3 of the samples is not selected, which is used to test the classification or regression effect of the current decision tree. In this study, we chose 1000 trees to calculate their importance.

C. UNet3+ for LIM

The framework of UNet3+ is shown in Fig. 4. As for LIM, full-scale skip connections and deep supervisions, derived from UNet3+ [42], are chosen to consider the multiscale characteristics and complex background of landslides. Encoder feature maps are concatenated with the same size, which is obtained by pool and bilinear up-sampling. With each decoder activated, the loss function reversely adjusts the weights of the network. In this study, the loss function coefficient of Dec_1 is 1, and the rest is 0.4.

Full-scale skip connections are used as an example for Dec_3, where Enc_1 and Enc_2 are downsampled by 4 times and 2 times, respectively, to unify the size of the feature maps. This was followed by 3×3 convolution with 64 channels. The feature map of the same scale encoder Enc_3 is directly operated with 3×3 convolution and 64 channels. Enc_4 and Enc_5 are upsampled 2 times and 4 times, respectively, also to ensure the uniformity of the feature map size, and the upsampling is done by bilinear interpolation.

The final feature map is generated by fusing the features of each decoding layer into a 3×3 convolutional layer, followed by a bilinear upsampling in order to return the feature map resolution to the input image. The segmentation results obtained after upsampling are multiplied with the results of the classification module. The result after multiplication is processed by sigmoid and the result obtained is the deeply supervised output.

Convolutional neural networks extract features of targets by layer-by-layer abstraction. The shallow network feature map has high resolution, rich spatial information, and weak semantic representation ability, which is suitable for dealing with small targets and highlighting landslide boundaries. The deep-layer network feature map has low resolution, weak geometric information representation, and strong semantic information representation, which is fit for dealing with large targets and locating the location of landslides. The image processing technique combining multiscale information can obtain deep semantic information and shallow geometric information, which can be applied to complex landslide mapping.

Due to the imbalance between landslide and nonlandslide (see Fig. 5), we choose focal loss (FL) [43] as the loss function of the network, based on the cross entropy (CE) as

$$CE(q, y) = \begin{cases} -\log(q) & y = 1 \\ -\log(1 - q) & y = 0 \end{cases} \quad (5)$$

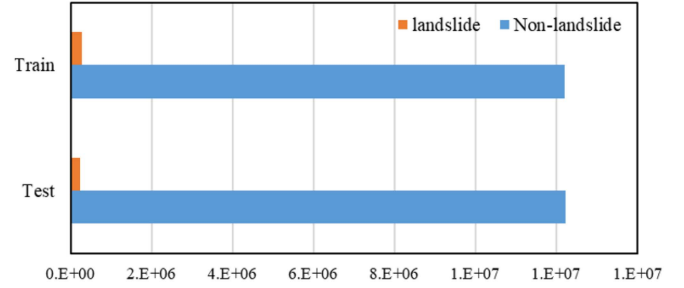


Fig. 5. Landslide and nonlandslide pixel statistics in the training and test areas.

where y is the predicted value of pixel, 0 represents nonlandslide, and 1 represents landslide. $q \in [0, 1]$ is the probability of landslide predicted by this pixel, which is inversely proportional to the loss value shown as

$$FL(qt) = -\alpha(1 - qt)^\gamma \log(qt). \quad (6)$$

Let $CE(q, y) = CE(qy)$, the weight contribution of landslide and nonlandslide samples to total loss is controlled by setting the value of α . A relatively small value of α is taken to reduce the weight of nonlandslide samples. $(1 - qt)^\gamma$ is called the focusing parameter, and $\gamma \geq 0$. By adjusting γ , the model focuses more on the difficult sample training. After experiments, α and γ are set as 0.3 and 1.5 in this study.

D. Quantitative Evaluation Index

We take recall, F1-score, and mIoU as evaluation model accuracy, which is derived from the confusion matrix. The four parameters of the confusion matrix are true positive (TP), true negative (TN), false positive (FP), and false negative (FN). In this study, TP refers to landslide output as landslide, TN refers to nonlandslide output as non-landslide, FP refers to nonlandslide output as landslide, and FN refers to landslide output as nonlandslide.

F1-score and recall are used to describe the classification quality comprehensively. mIoU represents the average value of the sum of each class, which is usually used to evaluate the model's ability in semantic segmentation

$$\text{Recall} = \frac{TP}{TP + FN} \quad (7)$$

$$\text{F1-score} = \frac{2 \times TP}{2 \times TP + FP + FN} \quad (8)$$

$$\text{mIoU} = \frac{1}{q+1} \sum_{i=0}^q \frac{TP}{TP + FP + FN} \quad (9)$$

$$\text{importance} = \frac{1}{n_{\text{tree}}} \sum_{i=1}^{n_{\text{tree}}} (\text{OOB2} - \text{OOB1}). \quad (10)$$

IV. RESULTS

A. Multifeatured Change Vector Analysis

As shown in Fig. 6(a), (b), and (c), we obtained the elevation, slope, and aspect from the DEM. In addition, we obtained NDVI

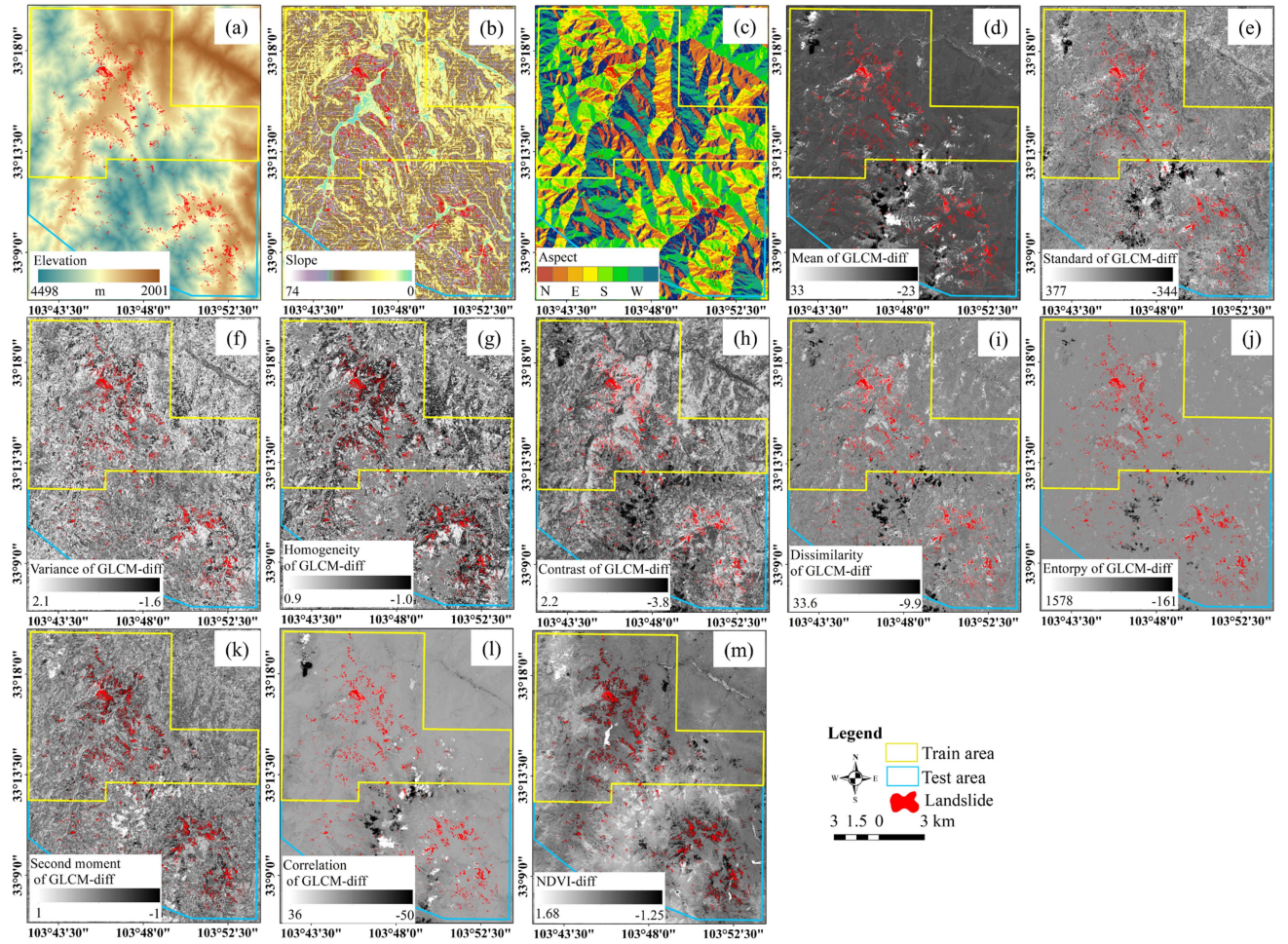


Fig. 6. Multifeature processing results. (a)–(c) Represent elevation, slope, and aspect obtained from DEM. (d)–(l) Represent the mean, standard, variance, homogeneity, contrast, dissimilarity, entropy, second moment, and correlation for GLCM processed by CVA, respectively. (m) Represents NDVI was processed with CVA.

and GLCM from pre- and postevent images, respectively. And the change values NDVI-diff [see Fig. 6(m)] and GLCM-diff [see Fig. 6(d)–(l)] were obtained by change vector analysis (CVA), where NDVI-diff indicates vegetation, a small value of change means a decrease in vegetation and a large value means an increase in vegetation. As can be seen in Fig. 6(m), most of the vegetation reduction areas overlap with the landslides, which is consistent with our interpretation on the optical images.

On the other hand, GLCM is used to describe the uniformity of the image grayscale distribution and the coarseness of the texture. From the variation values of different parameters of GLCM, it can be found that mean [see Fig. 6(d)], standard [see Fig. 6(e)], dissimilarity [see Fig. 6(i)], entropy [see Fig. 6(j)], and correlation [see Fig. 6(h)] are positively correlated with the degree of variation. Homogeneity [see Fig. 6(k)] is negatively correlated with the degree of variation. The rest of the values showed weak performance. Because the surface material was carried away by the debris to form a more regular form compared with the background features, the scars after the landslide show a simple and smooth image texture.

B. Feature Extraction Based on ICA and RFI

We extracted all features from landslides and nonlandslides, where nonlandslides were randomly generated with the equal number of landslides. Thirteen cofeatures (see Table I) were extracted for landslide points and nonlandslide points for feature processing and interpretation analysis.

This study used the RF package implemented by Scikit-learn in the Python programming environment for feature selection. The RFI ranking of the 13 features was shown in Fig. 7, where the three most important features were selected, i.e., the dissimilarity of GLCM (0.42), Elevation (0.21), and NDVI (0.053). Fig. 8(a), (b), and (c) shows dissimilarity, elevation, and NDVI, respectively. Fig. 8(d) is their false color map. Red, green, and blue channels are normalized NDVI, elevation, and dissimilarity, respectively. Landslides cause the loss of surface vegetation, resulting in strong changes in NDVI over a range of elevation. It can be seen that the selection characteristics of RFI are consistent with the occurrence of landslides. Visually, the dissimilarity also fits well with the label of landslide, and there are significant differences between landslides and nonlandslides.

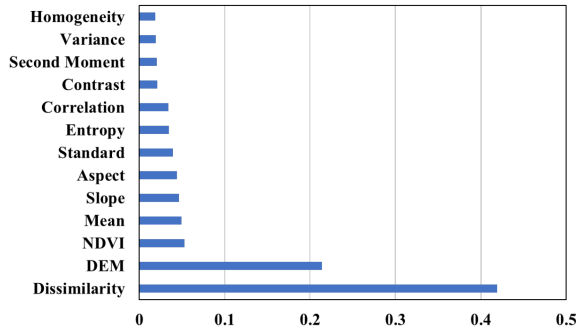


Fig. 7. Random forest importance of 13 features.

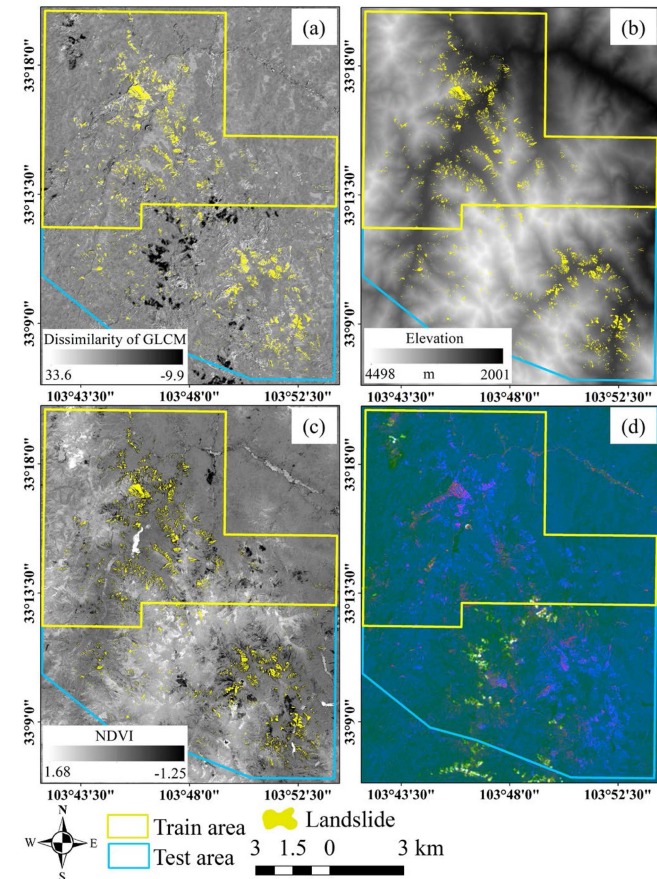


Fig. 8. Dissimilarity of GLCM-diff, elevation, NDVI-diff and false color image, respectively. (a), (b), and (c) are dissimilarity of GLCM, elevation, and NDVI, respectively. (d) Is false color image with normalized dissimilarity of GLCM, elevation, and NDVI.

ICA selects independent component 1 (IC1), independent component 2 (IC2), and independent component 3 (IC3) as co-features. Fig. 9 reveals that IC1 is very sensitive to change information, including seasonal noise, such as snow changes. IC2 fits well with landslides, and seasonal changes are isolated with low noise. IC3 has the most information, even some related to terrain. As can be seen in Fig. 9(d), the most prominent colors in the variation are very similar to landslides.

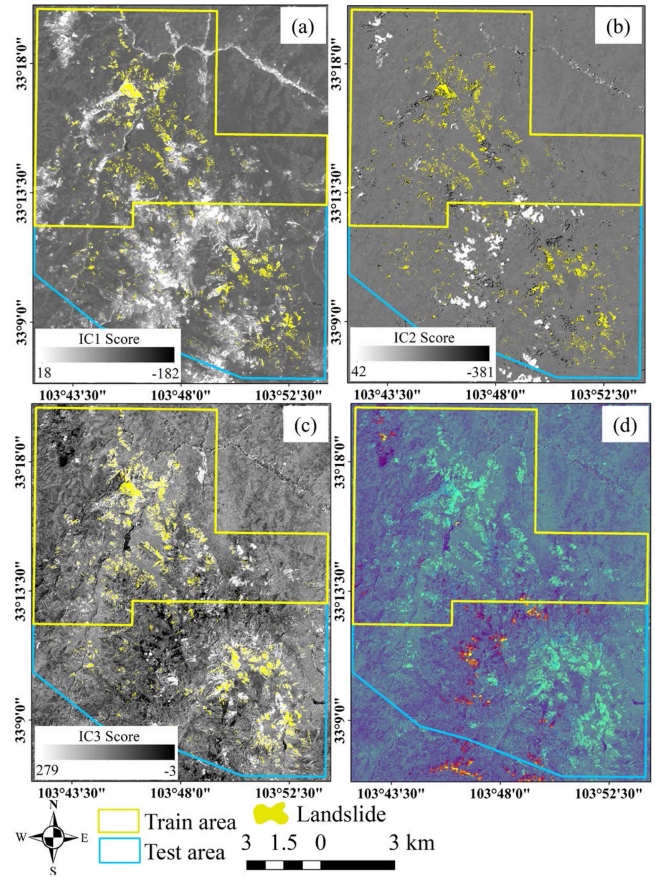


Fig. 9. Three independent components and false color map. (a) (b), and (c) are IC1, IC2, and IC3, respectively. (d) Is false color map of normalized IC1, IC2, and IC3.

TABLE II
QUANTITATIVE EVALUATION OF THREE METHODS

Method	Recall	F1	mIoU
UNet3+	0.5457	0.4791	0.6479
UNet3+ with RFI	0.6702	0.6161	0.7152
Proposed MICUNet3+ (UNet3+ with ICA)	0.6768	0.7027	0.7643

C. Quantitative Evaluation

The proposed MICUNet3+ has advantages in postevent image landslide recognition. The comparison of the indicators in Table II shows that all the indicators of the postevent image combination RFI and ICA are better than the postevent image recognition.

The accuracy of the postevent image assisted by ICA feature processing is the highest, with recall and F1-score distribution 0.13 and 0.22 higher than that of the postevent image only. The segmentation accuracy mIoU is also improved by 0.1164. Among the two feature processing methods of RFI and ICA, ICA has the best performance, i.e., the recall, F1 scores, and mIoU of ICA are 0.0066, 0.0866, and 0.0491 higher than those

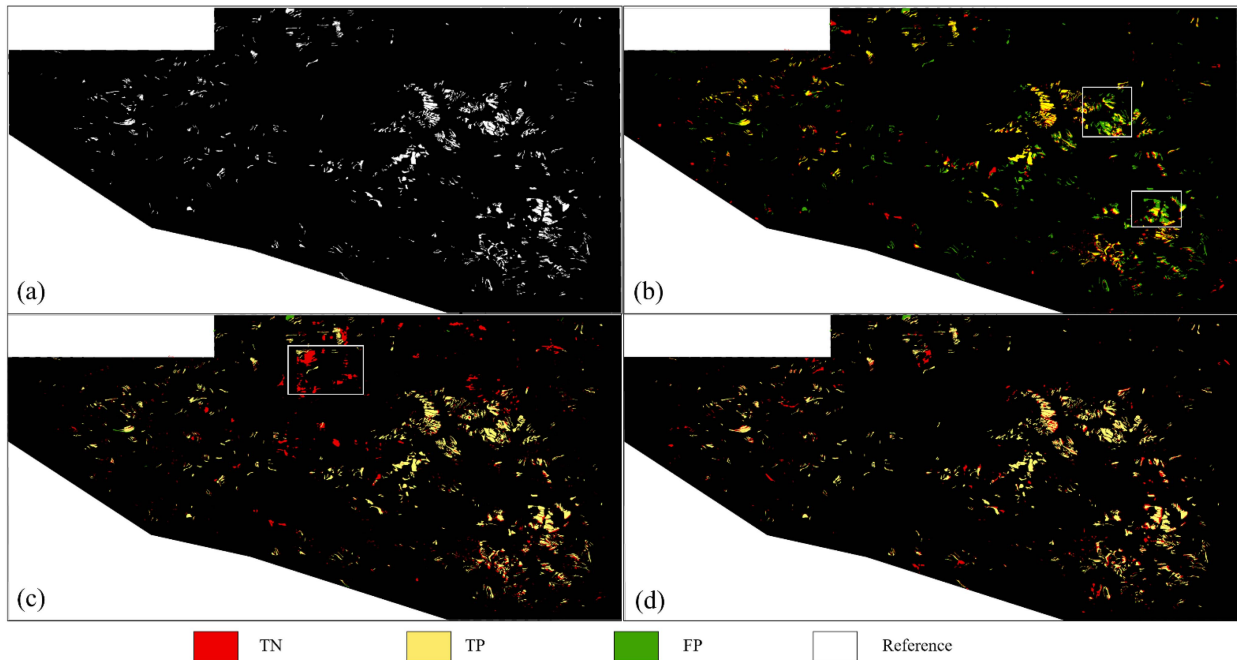


Fig. 10. Comparison of (a) reference, (b) UNet3+, (c) UNet3+ with RFI, (d) new proposed MICUNet3+ prediction results on test area of Jiuzhaigou earthquake driven landslides. The white boxes represent missed and incorrect tests.

of RFI. ICA is over 0.05 higher in overall evaluation and 0.03 higher in segmentation accuracy.

D. Qualitative Evaluation

Fig. 10 shows the prediction results of different methods, where Fig. 10(a)–(d) shows the reference and the results based on the UNet3+ network. Fig. 10(a) is the reference based on the visual interpretation, and Fig. 10(b) is the recognition results from the postevent image, which are only applicable to postevent images that are obvious. The segmentation results are not desirable due to the similarity of the landslide to other ground objects, resulting in more FPs in Fig. 10(b). Fig. 10(c) and (d) is the results of RFI- and ICA-assisted postevent images. The postevent images overlaid with the dissimilarity of GLCM, DEM, and NDVI selected by RFI can reduce FP, but generate more TN due to noise, as shown in Fig. 10(c). As shown in Table II, ICA is the most accurate one among the two feature processing methods. It can be seen from Fig. 10(d) that most of the predictions are consistent, although there is a small amount of TN in the prediction maps.

Overall, the cofeature selected by RFI improved the accuracy of landslide extraction and greatly reduced misclassification, but the noise introduced led to an increase in true negative. And ICA can largely solve this problem by improving the interclass heterogeneity and intraclass consistency.

Fig. 11 reveals the details of landslide mapping results assisted by RFI and ICA, where we can see that feature processing can assist the landslide mapping effectively, and different processing methods can get different landslide prediction results. Specifically, RFI has obvious misidentification phenomenon due to insufficient suppression of noise. Meanwhile, ICA can get best

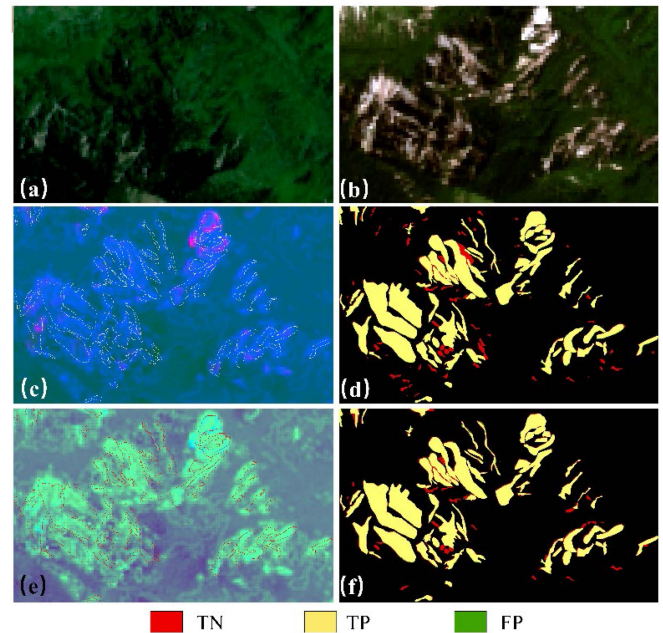


Fig. 11. Comparison of different feature processing methods. (a) and (b) are pre- and postevent image, respectively. (c) and (e) are false color maps of RFI and ICA, respectively. (d) and (f) are the prediction of UNet3+ with post+RFI and proposed MICUNet3+ methods.

segmentation results with no missing points and a small amount of misclassification.

V. DISCUSSION

The accuracy of landslide mapping can be improved by optical image derived information and topographic factors [32], [34],

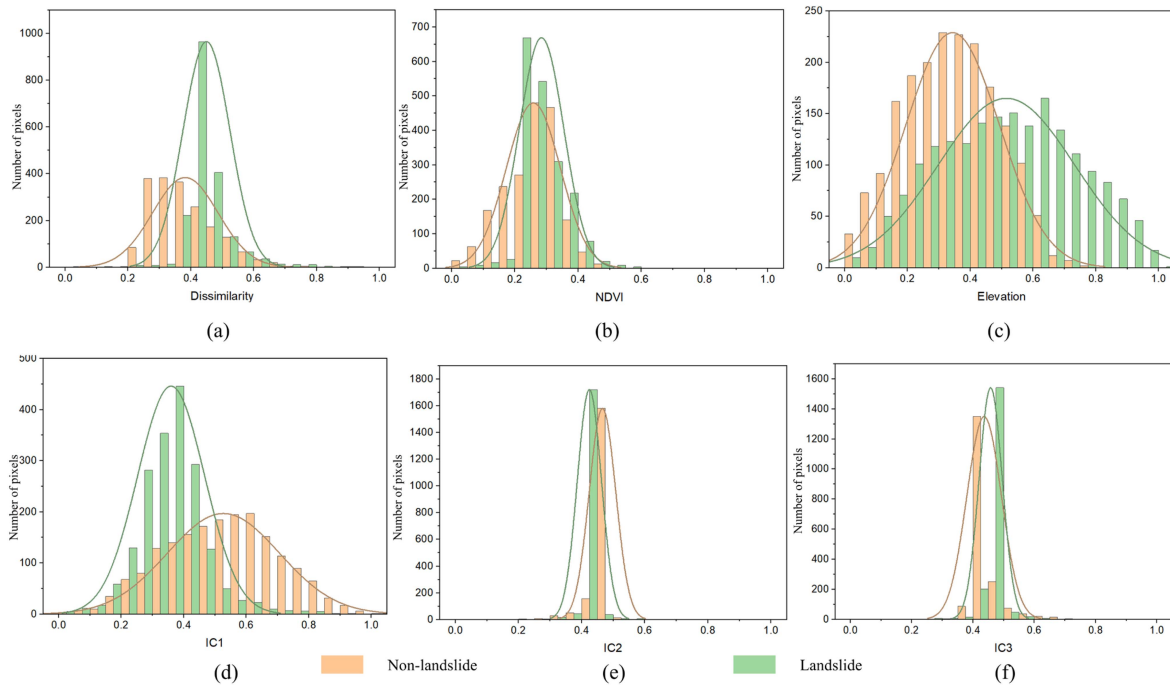


Fig. 12. Landslide and nonlandslide pixel statistics in three cofactors selected by RFI and three top principal components of ICA. (a)–(f) Represents the statistical number of landslide and non-landslide points, where (a) represents GLCM dissimilarity, (b) represents NDVI, (c) represents elevation, and (d)–(f) represent IC1.

[36]. In this study, a method is proposed for landslide inventory mapping using UNet3+ after ICA processing of multifactor assisted postevent images. Some issues still need to be discussed. There are some issues that still need to be discussed.

A. Multifeature Processing

Feature processing is to focus the classified features on several key features and to improve the intraclass homogeneity and interclass heterogeneity. In this study, we compared ICA and RFI in feature processing.

ICA is used to separate information by transforming the input space into maximally independent bases. Here, ICA can effectively suppress the multifeature noise, and retain the main change information, which is beneficial to landslide mapping driven by the events such as earthquake (see Table II).

ICA is different from feature selection, which is based on information entropy or Gini coefficient to select important features. RFI is a typical feature selection method. In this study, we compared the results of ICA and RFI and found that the former was more effective. The dissimilarity of GLCM, elevation, and NDVI selected by RFI could reflect the change information, but it is difficult to suppress the noise, which was reflected as the serious misclassification in the prediction maps of RFI-assisted postevent images [see Fig. 10(c)]. ICA reduces the noise in the original factor and increases the intraclass consistency and interclass heterogeneity. This is demonstrated by the statistical results, where we counted the three cofactors selected by RFI and the three top principal components of ICA using 2000 nonlandslides random points and 2000 landslides, respectively. Fig. 12(a), (b), and (c) is dissimilarity of GLCM, NDVI, and

elevation, respectively, and Fig. 12(d), (e), and (f) shows the top three principal components, respectively.

Based on the abovementioned discussion, we find that ICA can improve the intraclass homogeneity and enhance the interclass heterogeneity during the multifeature processing. Therefore, multifeature processed by ICA can effectively assist landslide mapping with postevent image.

B. Compared With Previous Work

The current research on deep learning in LIM focuses on both methods and data. Several scholars have studied the applicability of advanced deep learning modules to LIM. For example, residual modules, attention mechanisms, and transformer methods. Some other scholars have mainly studied the contribution of data to the accuracy improvement of deep learning LIM. For example, data preprocessing, data augmentation, cofactor, and data postprocessing.

The multifeatured processing of landslide samples by this study method MICUNet3+ is more significant in improving accuracy than network structure optimization. It is undeniable that network optimization needs to be more targeted according to the characteristics of the target.

C. Limitations and Future Work

There are some limitations to this study. The medium resolution optical images were used in this study, resulting in a low-resolution LIM. Second, in the data processing, we use only optical images, and no SAR or LiDAR images, which have the advantage of not being affected by clouds. In the model, we did not consider the influence of different backbone networks.

Currently, the network training takes a long time, so a more effective method needs to be found.

In the next study, we need to experiment with high-resolution data to extract more accurate weather landslides. We will consider extending this method to SAR and Lidar applications.

VI. CONCLUSION

In this article, we proposed a multifeatured MICUNet3+ method for coseismic landslide inventory mapping by combining ICA and UNet3+. We took Jiuzhaigou coseismic landslides as research region, where visually interpreted landslides were taken as samples to train, validation, and test our model. First, pre-earthquake Landsat-8 and postearthquake Sentinel-2 optical images with similar seasonal features and SRTM DEM were acquired. Then, optical images were preprocessed to derive features in terms of NDVI and 9 GLCM and DEM was preprocessed to derive features of slope and aspect. Next, NDVI and GLCM were processed by change vector analyses to obtain NDVI-diff and GLCM-diff, which were performed by ICA. We input IC1, IC2 and IC3 assisted images into UNet3+ for LIM. Results showed that our proposed MICUNet3+ performed well with complex background and multiscale features of landslides, as ICA can improve the intraclass homogeneity and interclass nonhomogeneity, which can provide a guideline for landslide identification under complex conditions.

However, due to the low image resolution, it is hardly to identify landslides with very small area. And the optical images are vulnerable to clouds to extract postearthquake landslides, which will affect the performance of our method. High resolution optical and SAR images will be further explored in subsequent studies to generate more accurate coseismic landslide inventory maps.

ACKNOWLEDGMENT

Sentinel-2 images were provided by European Space Agency (<https://www.esa.int/>) and Landsat-8 images were provided by U.S. Geological Survey (<https://www.usgs.gov/>). The landslide inventory map offered from the National Institute of Natural Hazards, Ministry of Emergency Management of China.

REFERENCES

- [1] J. Peng et al., "Heavy rainfall triggered loess-mudstone landslide and subsequent debris flow in Tianshui, China," *Eng. Geol.*, vol. 186, pp. 79–90, Feb. 2015, doi: [10.1016/j.enggeo.2014.08.015](https://doi.org/10.1016/j.enggeo.2014.08.015).
- [2] Y. Tian, C. Xu, S. Ma, X. Xu, S. Wang, and H. Zhang, "Inventory and spatial distribution of landslides triggered by the 8th August 2017 MW 6.5 Jiuzhaigou earthquake, China," *J. Earth Sci.*, vol. 30, no. 1, pp. 206–217, Feb. 2019, doi: [10.1007/s12583-018-0869-2](https://doi.org/10.1007/s12583-018-0869-2).
- [3] S. Zhang, L. M. Zhang, and T. Glade, "Characteristics of earthquake- and rain-induced landslides near the epicenter of Wenchuan earthquake," *Eng. Geol.*, vol. 175, pp. 58–73, Jun. 2014, doi: [10.1016/j.enggeo.2014.03.012](https://doi.org/10.1016/j.enggeo.2014.03.012).
- [4] B. Shan, Y. Zheng, C. Liu, Z. Xie, and J. Kong, "Coseismic Coulomb failure stress changes caused by the 2008 M7.0 Jiuzhaigou earthquake, and its relationship with the 2008 Wenchuan earthquake," *Sci. China Earth Sci.*, vol. 60, no. 12, pp. 2181–2189, Dec. 2017, doi: [10.1007/s11430-017-9125-2](https://doi.org/10.1007/s11430-017-9125-2).
- [5] T. Gorum, O. Korup, C. J. van Westen, M. van der Meijde, C. Xu, and F. D. van der Meer, "Why so few? Landslides triggered by the 2002 Denali earthquake, Alaska," *Quaternary Sci. Rev.*, vol. 95, pp. 80–94, Jul. 2014, doi: [10.1016/j.quascirev.2014.04.032](https://doi.org/10.1016/j.quascirev.2014.04.032).
- [6] U. Haque et al., "The human cost of global warming: Deadly landslides and their triggers (1995–2014)," *Sci. Total Environ.*, vol. 682, no. 1/2, pp. 673–684, 2019.
- [7] F. Guzzetti, A. C. Mondini, M. Cardinali, F. Fiorucci, M. Santangelo, and K.-T. Chang, "Landslide inventory maps: New tools for an old problem," *Earth-Sci. Rev.*, vol. 112, no. 1/2, pp. 42–66, Apr. 2012, doi: [10.1016/j.earscirev.2012.02.001](https://doi.org/10.1016/j.earscirev.2012.02.001).
- [8] P. Zhang, C. Xu, S. Ma, X. Shao, Y. Tian, and B. Wen, "Automatic extraction of seismic landslides in large areas with complex environments based on deep learning: An example of the 2018 Iburi earthquake, Japan," *Remote Sens.*, vol. 12, no. 23, Dec. 2020, Art. no. 3992, doi: [10.3390/rs12233992](https://doi.org/10.3390/rs12233992).
- [9] M. Bunn, B. Leshchinsky, M. Olsen, and A. Booth, "A simplified, object-based framework for efficient landslide inventories using LIDAR digital elevation model derivatives," *Remote Sens.*, vol. 11, no. 3, pp. 303–332, Feb. 2019, doi: [10.3390/rs11030303](https://doi.org/10.3390/rs11030303).
- [10] X. Liu et al., "Integration of Sentinel-1 and ALOS/PALSAR-2 SAR datasets for mapping active landslides along the Jinsha River corridor, China," *Eng. Geol.*, vol. 284, Apr. 2021, Art. no. 106033, doi: [10.1016/j.enggeo.2021.106033](https://doi.org/10.1016/j.enggeo.2021.106033).
- [11] C. Zhao and Z. Lu, "Remote sensing of landslides—A review," *Remote Sens.*, vol. 10, no. 2, pp. 279–285, Feb. 2018, doi: [10.3390/rs10020279](https://doi.org/10.3390/rs10020279).
- [12] S. Ling, C. Sun, X. Li, Y. Ren, J. Xu, and T. Huang, "Characterizing the distribution pattern and geologic and geomorphic controls on earthquake-triggered landslide occurrence during the 2017 Ms 7.0 Jiuzhaigou earthquake, Sichuan, China," *Landslides*, vol. 18, no. 4, pp. 1275–1291, Apr. 2021, doi: [10.1007/s10346-020-01549-6](https://doi.org/10.1007/s10346-020-01549-6).
- [13] J.-Y. Rau, L.-C. Chen, J.-K. Liu, and T.-H. Wu, "Dynamics monitoring and disaster assessment for watershed management using time-series satellite images," *IEEE Trans. Geosci. Remote Sens.*, vol. 45, no. 6, pp. 1641–1649, Jun. 2007, doi: [10.1109/TGRS.2007.894928](https://doi.org/10.1109/TGRS.2007.894928).
- [14] Z. Li, W. Shi, P. Lu, L. Yan, Q. Wang, and Z. Miao, "Landslide mapping from aerial photographs using change detection-based Markov random field," *Remote Sens. Environ.*, vol. 187, pp. 76–90, Dec. 2016, doi: [10.1016/j.rse.2016.10.008](https://doi.org/10.1016/j.rse.2016.10.008).
- [15] A. C. Mondini, F. Guzzetti, P. Reichenbach, M. Rossi, M. Cardinali, and F. Ardizzone, "Semi-automatic recognition and mapping of rainfall induced shallow landslides using optical satellite images," *Remote Sens. Environ.*, vol. 115, no. 7, pp. 1743–1757, Jul. 2011, doi: [10.1016/j.rse.2011.03.006](https://doi.org/10.1016/j.rse.2011.03.006).
- [16] D. Tien Bui et al., "Landslide detection and susceptibility mapping by AIRSAR data using support vector machine and index of entropy models in Cameron Highlands, Malaysia," *Remote Sens.*, vol. 10, no. 10, Sep. 2018, Art. no. 1527, doi: [10.3390/rs10101527](https://doi.org/10.3390/rs10101527).
- [17] A. Stumpf, J.-P. Malet, and C. Delacourt, "Correlation of satellite image time-series for the detection and monitoring of slow-moving landslides," *Remote Sens. Environ.*, vol. 189, pp. 40–55, Feb. 2017, doi: [10.1016/j.rse.2016.11.007](https://doi.org/10.1016/j.rse.2016.11.007).
- [18] T. Chen, J. Trinder, and R. Niu, "Object-oriented landslide mapping using ZY-3 satellite imagery, random forest and mathematical morphology, for the Three-Gorges Reservoir, China," *Remote Sens.*, vol. 9, no. 4, pp. 333–347, Mar. 2017, doi: [10.3390/rs9040333](https://doi.org/10.3390/rs9040333).
- [19] R. Behling, S. Roessner, H. Kaufmann, and B. Kleinschmit, "Automated spatiotemporal landslide mapping over large areas using RapidEye time series data," *Remote Sens.*, vol. 6, no. 9, pp. 8026–8055, Aug. 2014, doi: [10.3390/rs6098026](https://doi.org/10.3390/rs6098026).
- [20] A. Mohan, A. K. Singh, B. Kumar, and R. Dwivedi, "Review on remote sensing methods for landslide detection using machine and deep learning," *Trans. Emerg. Telecommun. Technol.*, vol. 32, no. 7, Jul. 2021, Art. no. e3998, doi: [10.1002/ett.3998](https://doi.org/10.1002/ett.3998).
- [21] L. Zhang, L. Zhang, and B. Du, "Deep learning for remote sensing data: A technical tutorial on the state of the art," *IEEE Geosci. Remote Sens. Mag.*, vol. 4, no. 2, pp. 22–40, Jun. 2016, doi: [10.1109/MGRS.2016.2540798](https://doi.org/10.1109/MGRS.2016.2540798).
- [22] O. Ghorbanzadeh, T. Blaschke, K. Gholamnia, S. Meena, D. Tiede, and J. Aryal, "Evaluation of different machine learning methods and deep learning convolutional neural networks for landslide detection," *Remote Sens.*, vol. 11, no. 2, pp. 196–217, Jan. 2019, doi: [10.3390/rs11020196](https://doi.org/10.3390/rs11020196).
- [23] S. R. Meena et al., "Rapid mapping of landslides in the Western Ghats (India) triggered by 2018 extreme monsoon rainfall using a deep learning approach," *Landslides*, vol. 18, no. 5, pp. 1937–1950, May 2021, doi: [10.1007/s10346-020-01602-4](https://doi.org/10.1007/s10346-020-01602-4).

- [24] S. Ji, D. Yu, C. Shen, W. Li, and Q. Xu, "Landslide detection from an open satellite imagery and digital elevation model dataset using attention boosted convolutional neural networks," *Landslides*, vol. 17, no. 6, pp. 1337–1352, Jun. 2020, doi: [10.1007/s10346-020-01353-2](https://doi.org/10.1007/s10346-020-01353-2).
- [25] Y. Yi and W. Zhang, "A new deep-learning-based approach for earthquake-triggered landslide detection from single-temporal RapidEye satellite imagery," *IEEE J. Sel. Topics Appl. Earth Observ. Remote Sens.*, vol. 13, pp. 6166–6176, Oct. 2020, doi: [10.1109/JSTARS.2020.3028855](https://doi.org/10.1109/JSTARS.2020.3028855).
- [26] W. Shi, M. Zhang, H. Ke, X. Fang, Z. Zhan, and S. Chen, "Landslide recognition by deep convolutional neural network and change detection," *IEEE Trans. Geosci. Remote Sens.*, vol. 59, no. 6, pp. 4654–4672, Jun. 2021, doi: [10.1109/TGRS.2020.3015826](https://doi.org/10.1109/TGRS.2020.3015826).
- [27] W. Qi, M. Wei, W. Yang, C. Xu, and C. Ma, "Automatic mapping of landslides by the ResU-Net," *Remote Sens.*, vol. 12, no. 15, Aug. 2020, Art. no. 2487, doi: [10.3390/rs12152487](https://doi.org/10.3390/rs12152487).
- [28] P. Liu, Y. Wei, Q. Wang, Y. Chen, and J. Xie, "Research on post-earthquake landslide extraction algorithm based on improved U-Net model," *Remote Sens.*, vol. 12, no. 5, p. 894, Mar. 2020, doi: [10.3390/rs12050894](https://doi.org/10.3390/rs12050894).
- [29] L. Nava, K. Bhuyan, S. R. Meena, O. Monserrat, and F. Catani, "Rapid mapping of landslides on SAR data by attention U-Net," *Remote Sens.*, vol. 14, no. 6, Mar. 2022, Art. no. 1449, doi: [10.3390/rs14061449](https://doi.org/10.3390/rs14061449).
- [30] D. Tuia, R. Roscher, J. D. Wegner, N. Jacobs, X. Zhu, and G. Camps-Valls, "Towards a collective agenda on AI for Earth science data analysis," *IEEE Geosci. Remote Sens. Mag.*, vol. 9, no. 2, pp. 88–104, Jun. 2021, doi: [10.1109/MGRS.2020.3043504](https://doi.org/10.1109/MGRS.2020.3043504).
- [31] Q. Yuan et al., "Deep learning in environmental remote sensing: Achievements and challenges," *Remote Sens. Environ.*, vol. 241, May 2020, Art. no. 111716, doi: [10.1016/j.rse.2020.111716](https://doi.org/10.1016/j.rse.2020.111716).
- [32] X. Gao, T. Chen, R. Niu, and A. Plaza, "Recognition and mapping of landslide using a fully convolutional DenseNet and influencing factors," *IEEE J. Sel. Topics Appl. Earth Observ. Remote Sens.*, vol. 14, pp. 7881–7894, Aug. 2021, doi: [10.1109/JSTARS.2021.3101203](https://doi.org/10.1109/JSTARS.2021.3101203).
- [33] L. P. Soares, H. C. Dias, G. P. B. Garcia, and C. H. Grohmann, "Landslide segmentation with deep learning: Evaluating model generalization in rainfall-induced landslides in Brazil," *Remote Sens.*, vol. 14, no. 9, May 2022, Art. no. 2237, doi: [10.3390/rs14092237](https://doi.org/10.3390/rs14092237).
- [34] R. Yang, F. Zhang, J. Xia, and C. Wu, "Landslide extraction using mask R-CNN with background-enhancement method," *Remote Sens.*, vol. 14, no. 9, May 2022, Art. no. 2206, doi: [10.3390/rs14092206](https://doi.org/10.3390/rs14092206).
- [35] H. Chen et al., "A landslide extraction method of channel attention mechanism U-Net network based on Sentinel-2A remote sensing images," *Int. J. Digit. Earth*, vol. 16, no. 1, pp. 552–577, Mar. 2023, doi: [10.1080/17538947.2023.2177359](https://doi.org/10.1080/17538947.2023.2177359).
- [36] O. Ghorbanzadeh, S. R. Meena, H. Shahabi Sorman Abadi, S. Tavakkoli Pirailou, L. Zhiyong, and T. Blaschke, "Landslide mapping using two main deep-learning convolution neural network streams combined by the Dempster-Shafer model," *IEEE J. Sel. Topics Appl. Earth Observ. Remote Sens.*, vol. 14, pp. 452–463, Dec. 2021, doi: [10.1109/JSTARS.2020.3043836](https://doi.org/10.1109/JSTARS.2020.3043836).
- [37] X. Wang, X. Fan, Q. Xu, and P. Du, "Change detection-based coseismic landslide mapping through extended morphological profiles and ensemble strategy," *Int. Soc. Photogrammetry Remote Sens. J. Photogrammetry Remote Sens.*, vol. 187, pp. 225–239, May 2022, doi: [10.1016/j.isprsjprs.2022.03.011](https://doi.org/10.1016/j.isprsjprs.2022.03.011).
- [38] Y. Li, C. Huang, S. Yi, and C. Wu, "Study on seismic fault and source rupture tectonic dynamic mechanism of Jiuzhaigou Ms7.0 earthquake," *J. Eng. Geol.*, vol. 25, no. 4, pp. 1141–1150, 2017.
- [39] T.-W. Lee, M. Girolami, A. J. Bell, and T. J. Sejnowski, "A unifying information-theoretic framework for independent component analysis," *Comput. Math. Appl.*, vol. 39, no. 11, pp. 1–21, Jun. 2000, doi: [10.1016/S0898-1221\(00\)00101-2](https://doi.org/10.1016/S0898-1221(00)00101-2).
- [40] L. Breiman, "Random forests," *Mach. Learn.*, vol. 45, no. 1, pp. 5–32, 2001.
- [41] P. Wei, Z. Lu, and J. Song, "Variable importance analysis: A comprehensive review," *Rel. Eng. Syst. Saf.*, vol. 142, pp. 399–432, Oct. 2015, doi: [10.1016/j.ress.2015.05.018](https://doi.org/10.1016/j.ress.2015.05.018).
- [42] H. Huang et al., "UNet 3+: A full-scale connected UNet for medical image segmentation," in *Proc. IEEE Int. Conf. Acoust., Speech Signal Process.*, 2020, pp. 1055–1059, doi: [10.1109/ICASSP40776.2020.9053405](https://doi.org/10.1109/ICASSP40776.2020.9053405).
- [43] X.-Y. Jing et al., "Multiset feature learning for highly imbalanced data classification," *IEEE Trans. Pattern Anal. Mach. Intell.*, vol. 43, no. 1, pp. 139–156, Jan. 2021, doi: [10.1109/TPAMI.2019.2929166](https://doi.org/10.1109/TPAMI.2019.2929166).



Xuerong Chen (Student Member, IEEE) received the B.S. degree in surveying and mapping engineering in 2014 from Chang'an University, Xi'an, China, where she is currently working toward the Ph.D. degree in geodesy and surveying engineering.

Her research interests include multisource remote sensing data and deep learning to identify geological hazards.



Chaoying Zhao (Senior Member, IEEE) received the M.S. and Ph.D. degrees in geodesy and surveying engineering from Chang'an University, Xi'an, China, in 2002 and 2009, respectively.

He is currently a Professor of geodesy and survey engineering with Chang'an University. His research interests include the development of different InSAR methods, including dynamic SAR/InSAR data processing with the sequential least-squares norm, large gradient surface deformation with SAR offset tracking method, and their applications in geohazard identification, monitoring, and mechanism explanations, including land subsidence, ground fissures, landslide, and mining-induced collapse.



Zhong Lu (Senior Member, IEEE) received the B.S. and M.S. degrees from Peking University, Beijing, China, in 1989 and 1992, respectively, and the Ph.D. degree from the University of Alaska, Fairbanks, AK, USA, in 1996, all in geophysics.

He is currently a Professor and the Endowed Shuler-Foscue Chair with the Huffington Department of Earth Sciences, Southern Methodist University, Dallas, TX, USA. He is also a Principal Investigator of projects funded by NASA, ESA, JAXA, DLR, and USGS on the study of land surface deformation

using satellite interferometric synthetic aperture radar (InSAR) imagery. He has authored more than 45 and coauthored 90 peer-reviewed journal articles and book chapters focused on InSAR techniques and applications. His research interests include technique developments of SAR, InSAR, and their applications on natural hazard monitoring and natural resource characterization.



Jiangbo Xi (Member, IEEE) received the B.S. degree in electronic and information science and technology from Jilin University, Changchun, China, in 2008, the Ph.D. degree in signal and information processing from the University of Chinese Academy of Sciences, Beijing, China, in 2017, and the joint Ph.D. degree in electrical and computer engineering from Purdue University, West Lafayette, IN, USA, in April 2017.

He is currently an Associate Professor with the School of Geology Engineering and Geomatics, Chang'an University, China. His current research

interests include deep learning, machine learning, landslide recognition, and objects detection in optical sequential images.